Statistics of active and passive scalars in one-dimensional compressible turbulence

Qionglin Ni* and Shiyi Chen

State Key Laboratory of Turbulence and Complex Systems, Center for Applied Physics and Technology, and Key Laboratory of High Energy Density Physics Simulation, Ministry of Education, College of Engineering, Peking University, 100871, Beijing, People's Republic of China

(Received 9 September 2012; revised manuscript received 13 November 2012; published 12 December 2012)

Statistics of the active temperature and passive concentration advected by the one-dimensional stationary compressible turbulence at $\mathrm{Re}_\lambda = 2.56 \times 10^6$ and $M_t = 1.0$ is investigated by using direct numerical simulation with all-scale forcing. It is observed that the signal of velocity, as well as the two scalars, is full of small-scale sawtooth structures. The temperature spectrum corresponds to $G(k) \propto k^{-5/3}$, whereas the concentration spectrum acts as a double power law of $H(k) \propto k^{-5/3}$ and $H(k) \propto k^{-7/3}$. The probability distribution functions (PDFs) for the two scalar increments show that both δT and δC are strongly intermittent at small separation distance r and gradually approach the Gaussian distribution as r increases. Simultaneously, the exponent values of the PDF tails for the large negative scalar gradients are $q_\theta = -4.0$ and $q_\zeta = -3.0$, respectively. A single power-law region of finite width is identified in the structure function (SF) of δT; however, in the SF of δC, there are two regions with the exponents taken as a local minimum and a local maximum. As for the scalings of the two SFs, they are close to the Burgers and Obukhov-Corrsin scalings, respectively. Moreover, the negative filtered flux at large scales and the time-increasing total variance give evidences to the existence of an inverse cascade of the passive concentration, which is induced by the implosive collapse in the Lagrangian trajectories.

DOI: 10.1103/PhysRevE.86.066307 PACS number(s): 47.40.−x, 47.10.ad, 47.27.Gs

I. INTRODUCTION

The one-dimensional (1D) randomly forced Burgers equation

$$\partial_t u + u\partial_x u = \nu\partial_x^2 u + f, \tag{1.1}$$

among the simplest theoretical models in the nonequilibrium statistical mechanics, is often served as a model for turbulence without pressure [1–13]. More precisely, when driven by the white-in-time, zero-mean force added at large scales, the Burgers flow is dominated by shocks, leading to the energy spectrum $E(k) \propto k^{-2}$ and the velocity structure function (SF) $S_p(r) =< |\delta u|^p > \propto r^1$ at $p \geqslant 1$ [1,14,15]. Totally different $E(k)$ and $S_p(r)$ are obtained when the force becomes all-scale and its formula in spectra space satisfies [2]

$$\langle \widehat{f}(k,t)\widehat{f}(k',t')\rangle = 2(2\pi)^2 Dk^{-1}\delta(k+k')\delta(t-t'), \tag{1.2}$$

where the circumflex denotes the Fourier representation. It corresponds to the almost constant energy flux $\Pi(k) \propto \ln(k/k_0)$, where k_0 is the largest allowed wave number. Simulations on this all-scale forced Burgers flow give that $E(k) \propto k^{-5/3}$, characteristic of Kolmogorov turbulence. But $S_p(r)$ shows strong deviations from the Kolmogorov picture, it is $S_{p\geqslant 3} \propto r^1$, characteristic of shocks [2,3,16]. In a word, this Burgers flow has both normal spectrum and anomalous scaling.

The scalar advected by compressible hydrodynamic turbulence is of fundamental importance in many problems ranging from astrophysics [17] to combustion [18], because it is the compressible rather than the Burgers turbulence arising in a large number of applications such as supersonic combustion, interplanet space exploration, and star-forming clouds [19]. Therefore, in this paper, we carry out a numerical investigation on the statistical behaviors of temperature and concentration in the 1D compressible Navier-Stokes (NS) turbulence forced by Eq. (1.2). Although both temperature and concentration are scalars advected by the same velocity, their properties are quite different. The temperature influences the velocity, as through the buoyancy force [20], then is named as an active scalar. Conversely, the concentration is a passive scalar because its feedback on the velocity is negligible. This means that the passive concentration belongs to the realm of linear problems, whereas the active temperature coupling the velocity makes the problem fully nonlinear [20].

Moreover, on the influence of the strong compressibility of the 1D compressible flow, the Lagrangian trajectories of the passive concentration collapse implosively, leading to the appearance of the upscale inverse cascade in the flux transfer [21–23]. The remainder of this paper is organized as follows. In Sec. II we describe the numerical schemes and simulated parameters, and then the basic properties of the 1D compressible flow. The statistics of temperature and concentration, including various probability distribution functions (PDFs), SFs, scaling exponents, and spectra, are analyzed in Sec. III. In Sec. IV, we give a summary and discussion.

II. NUMERICAL SCHEMES AND BASIC FLOW PROPERTIES

The numerical schemes for constructing the 1D compressible flow are the seventh-order Weighted Essentially Non-Oscillatory (WENO) method [24] for space discretization and the third-order total variation diminishing (TVD) Runge-Kutta method [25] for time advancement. By introducing the scales of length L, velocity U, temperature T_0, density ρ_0, dynamic viscosity μ_0, thermal conductivity κ_0, and molecular diffusivity χ_0, the dimensionless form of governing equations are written as

$$\partial_t \rho + \partial_x(\rho u) = 0, \tag{2.1}$$

*niql.pku@gmail.com

$$\partial_t(\rho u) + \partial_x\left(\rho u^2 + \frac{p}{\gamma M^2}\right) - \frac{1}{\mathrm{Re}}\partial_x(\mu\partial_x u) = \rho f_u, \quad (2.2)$$

$$\partial_t\mathcal{E} + \partial_x\left[(\mathcal{E} + \frac{p}{\gamma M^2})u\right] - \frac{1}{\mathrm{Re}}\partial_x[(\mu\partial_x u)u] - \frac{1}{\alpha}\partial_x(\kappa\partial_x T) = \rho u f_u, \quad (2.3)$$

$$\partial_t(\rho C) + \partial_x(\rho u C) - \frac{\gamma M^2}{\alpha}\partial_x(\chi\partial_x C) = \rho f_C, \quad (2.4)$$

$$p = \rho T, \quad (2.5)$$

where ρ, u, T, and C are for density, velocity, temperature, and concentration, respectively, and the total energy per unit volume $\mathcal{E}$ is

$$\mathcal{E} = \frac{p}{(\gamma-1)\gamma M^2} + \frac{\rho u^2}{2}. \quad (2.6)$$

Here, $\alpha \equiv \mathrm{RePr}(\gamma-1)M^2$, $\mathrm{Re} \equiv \rho_0 U L/\mu_0$ is the Reynolds number, $\mathrm{Pr} \equiv \mu_0 \mathrm{C_p}/\kappa_0$ is the Prandtl number with value of 0.7, C_p is the heat capacity at constant pressure. $M \equiv U/c_0$ is the reference Mach number, $c_0 = \sqrt{\gamma R T_0}$ is the sound speed, R is the gas constant, γ is the adiabatic exponent of gas and its value is set as 1.4.

We employ the Sutherland's law [26] to specify the temperature-dependent dynamic viscosity, thermal conductivity, and molecular diffusivity. Their dimensionless forms are

$$\mu,\kappa,\chi = \frac{1.4042T^{1.5}}{T + 0.40417}. \quad (2.7)$$

The randomly driving forces f_u and f_C are two independent realizations of the same formula. In other words, they are both white-in-time, zero mean, and their expressions in Fourier space are as follows [2,16]:

$$\widehat{f}_{\{u,C\}}(k,t) = \frac{A_f k^{-s/2}\sigma_k}{\sqrt{dt}} \quad k \leqslant k_c;$$
$$\widehat{f}_{\{u,C\}}(k,t) = 0 \quad k > k_c, \quad (2.8)$$

where σ_k is a Gaussian random variable with zero mean and unity covariance, $s = 1.0$, and $A_f = \sqrt{2}\times 10^{-3}$, $dt = 5.0 \times 10^{-6}$ is the time step. The cutoff wave number $k_c = 20480$ is chosen well inside the dissipation range of energy spectrum. In the simulation, we use the periodic boundary condition of $x \in [0,2\pi]$ and the initial fields of $\{\rho,u,T,C\}(x,0) = \{1.0,1.0,1.0,1.0\}$. The grid resolution is set as $N = 192\,000$. Moreover, the 1D compressible flow is characterized by two basic parameters, namely, the Taylor microscale Re_λ and turbulent Mach number M_t, defined as

$$\mathrm{Re}_\lambda = \frac{u'\lambda\rho}{\langle\mu\rangle}, \quad (2.9)$$

$$M_t = \frac{Mu'}{\sqrt{T}}, \quad (2.10)$$

where u' is the root-mean-square (r.m.s.) component fluctuating velocity and $\lambda = u'/\sqrt{(\partial_x u)^2}$ is the Taylor microscale. The definitions of other simulated parameters such as the energy spectrum $E(k)$, integral length scale L_I, Kolmogorov length scale η, and viscous dissipation rate ϵ are as follows:

$$\int_0^\infty E(k)dk = \frac{1}{2}u'^2, \quad (2.11)$$

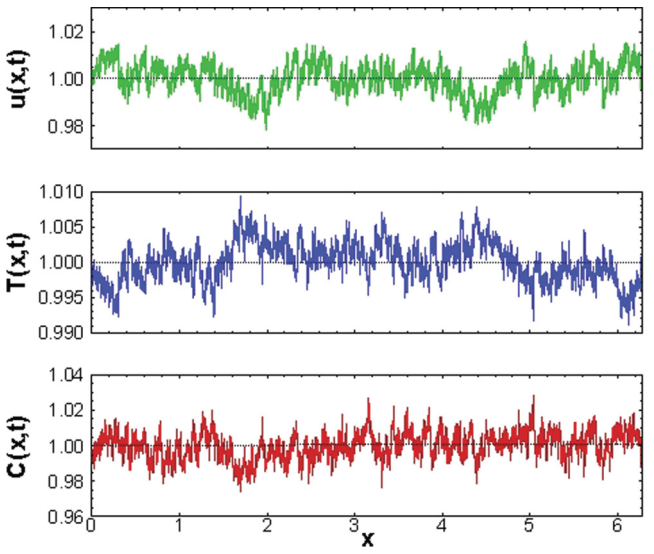

FIG. 1. (Color online) The signals of velocity (top), temperature (middle), and concentration (bottom) in the 1D compressible turbulence at time $t = 5.0$ (solid lines) and $t = 0$ (dotted lines, the initial data).

$$L_I = \frac{1}{\langle u(x,t)^2\rangle}\int_0^\infty \langle u(x,t)u(x+r,t)\rangle dr, \quad (2.12)$$

$$\eta = \left\langle\frac{\mu^3}{\rho^3\epsilon}\right\rangle^{1/4}, \quad (2.13)$$

$$\epsilon = \frac{1}{\mathrm{Re}}\left\langle\frac{\mu}{\rho}\xi^2\right\rangle. \quad (2.14)$$

The stationary state of the 1D compressible flow is achieved for the first time at $t_0 = 3.4$. The time-averaged values of the Taylor Reynolds number and turbulent Mach number in the stationary state are $\mathrm{Re}_\lambda = 2.56\times 10^6$ and $M_t = 1.0$. In Fig. 1, we plot the stationary signals of the 1D compressible flow at time $t = 5.0$. It is seen that the velocity, temperature, and concentration are all full of the small-scale sawtooth structures, which also appear in the Burgers turbulence driven by the same style random force [2,3,16]. All these signals are superimposed by the fluctuating components around their initial data. We notice that the stationary velocity is consistent of a few large-amplitude shocks and many small-amplitude ones. As time progresses, these shocks may merge into a single strong shock, but the subsequent breakdown makes it change into several smaller ones again. In Fig. 2 we plot $\rho^{\gamma-1}$ versus T, showing that all data collapse onto the solid line, implying that the isentropic condition is approximately valid in the 1D all-scale forced compressible flow, which is similar to that in Ref. [27]. The time-averaged energy spectrum is plotted in Fig. 3. We observe that in an inertial range of about two decades, the Kolmogorov $k^{-5/3}$ spectrum is reproduced.

III. NUMERICAL RESULTS

A. Probability distribution function

Figure 4 shows the time-averaged normalized PDFs for the fluctuating components of velocity, temperature and concentration, where u'_{rms}, T'_{rms} and C'_{rms} are the r.m.s. fluctuations.

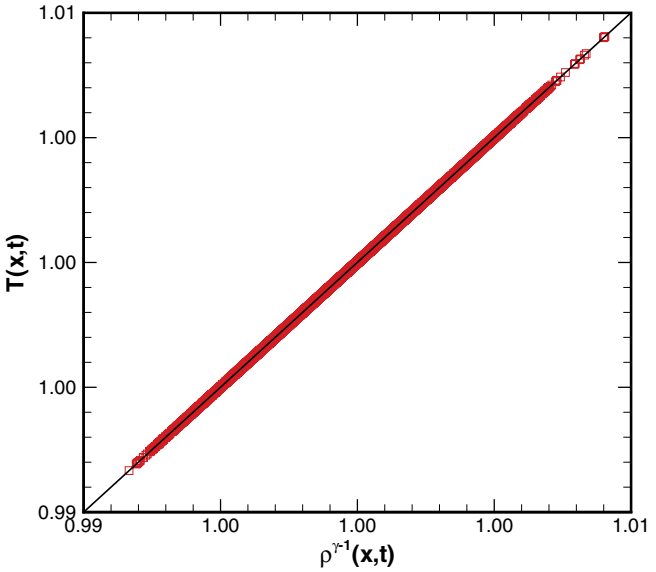

FIG. 2. (Color online) $\rho^{\gamma-1}$ versus T, 1920 points are used in the plot. The solid line is for the isentropic relationship.

The Gaussian distribution is plotted for comparison. We observe that these PDFs are all near Gaussian at small amplitudes and decay faster than Gaussian at large amplitudes. This means that the tails of the PDFs are sub-Gaussian, which is in agreement with the sub-Gaussian PDFs of scalars in the three-dimensional (3D) NS flow [28,29] but contrasted to the super-Gaussian PDFs of scalars in the Kraichnan flow [20,28,30–32].

To see how the distributions of the velocity and scalars change with increase in scale, we plot in Fig. 5 the PDFs for the normalized velocity, temperature and concentration increments (i.e., $\delta u/\sigma_{\delta u}$, $\delta T/\sigma_{\delta T}$, $\delta C/\sigma_{\delta C}$) at different separation distances. At the small normalized separation distance r/η, the left and right long tails in these PDFs imply the existence of strong intermittencies for $\delta u < 0$, $\delta C < 0$, and $\delta T > 0$,

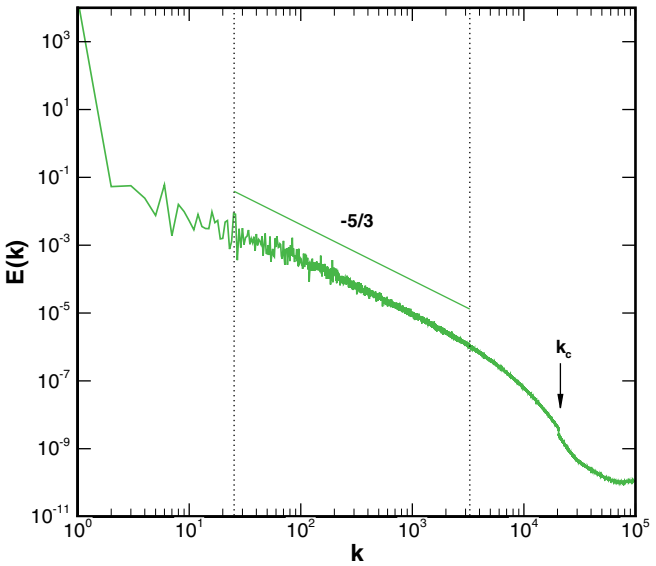

FIG. 3. (Color online) The energy spectrum $E(k)$, where k_c is for the cutoff wave number of f_u.

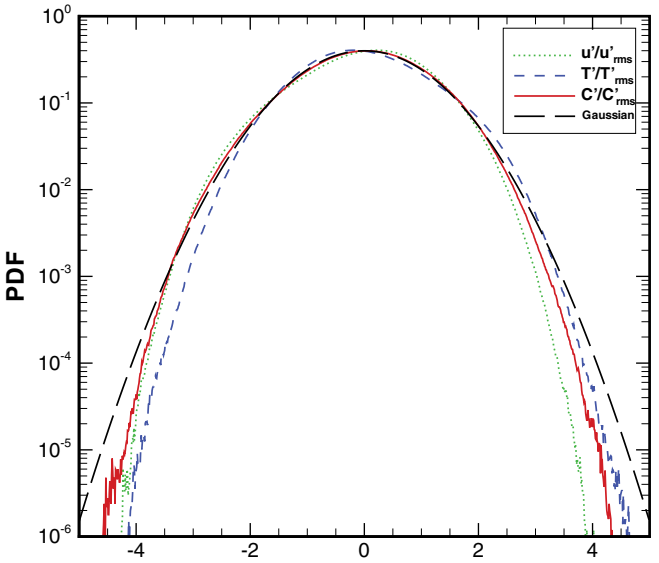

FIG. 4. (Color online) The PDFs for velocity (dotted line), temperature (dashed line), and concentration (solid line) normalized by their standard deviations. The long dashed line is for the Gaussian PDF.

respectively. The PDF tails for the three increments are all concave at large amplitudes. This feature is consistent with the scalar PDFs observed the experimental measurements. As r/η increases, the PDFs are more and more narrow and become Gaussian at $r/\eta = 2048$.

The change of the distributions of velocity and scalar increments can be characterized by the skewness and flatness as well. For example, those for δu are defined as follows [29]:

$$\mathcal{S}_{\delta u} = \frac{\langle \delta u^3 \rangle}{\langle \delta u^2 \rangle^{3/2}}, \qquad \mathcal{K}_{\delta u} = \frac{\langle \delta u^4 \rangle}{\langle \delta u^2 \rangle^2}, \tag{3.1}$$

where $\langle \cdot \rangle$ denotes ensemble average. Similar definitions are for δT and δC. In Fig. 6, we plot the three skewnesses against r/η. It shows that $\mathcal{S}_{\delta u}$ and $\mathcal{S}_{\delta C}$ are negative and their local minima are -11.06 and -6.62, respectively, whereas $\mathcal{S}_{\delta T}$ is positive and its local maximum is 9.57. As r/η increases, the magnitudes of these skewnesses decrease rapidly and approach zero, implying that when r is large enough, δu, δT, and δC all recover to the Gaussian distribution. Additionally, the magnitude of $\mathcal{S}_{\delta C}$ is smaller than that of $\mathcal{S}_{\delta u}$ throughout the whole r/η range, especially for the small range, indicating that the mean flux of concentration transferring to the small scales is smaller than that of velocity. Figure 7 shows that the curves for δu and δT are overlapped, giving $\mathcal{K}_{\delta u} = \mathcal{K}_{\delta T}$. Moreover, the three flatnesses all increase rapidly as r/η decreases, implying the increase in the intermittencies of δu, δT, and δC. In the range of $r/\eta < 750$, $\mathcal{K}_{\delta C}$ is smaller than both $\mathcal{K}_{\delta u}$ and $\mathcal{K}_{\delta T}$, whereas they are nearly the same in the larger-scale range. The detailed variation in flatness against r/η is plotted in the inset. It shows that as r/η increases, all the flatnesses approach three, the Gaussian distribution with no intermittency.

In Fig. 8, we plot the time-averaged normalized PDFs for the normalized velocity, temperature, and concentration gradients (i.e., ξ/σ_ξ, θ/σ_θ, ζ/σ_ζ). It is seen that the three

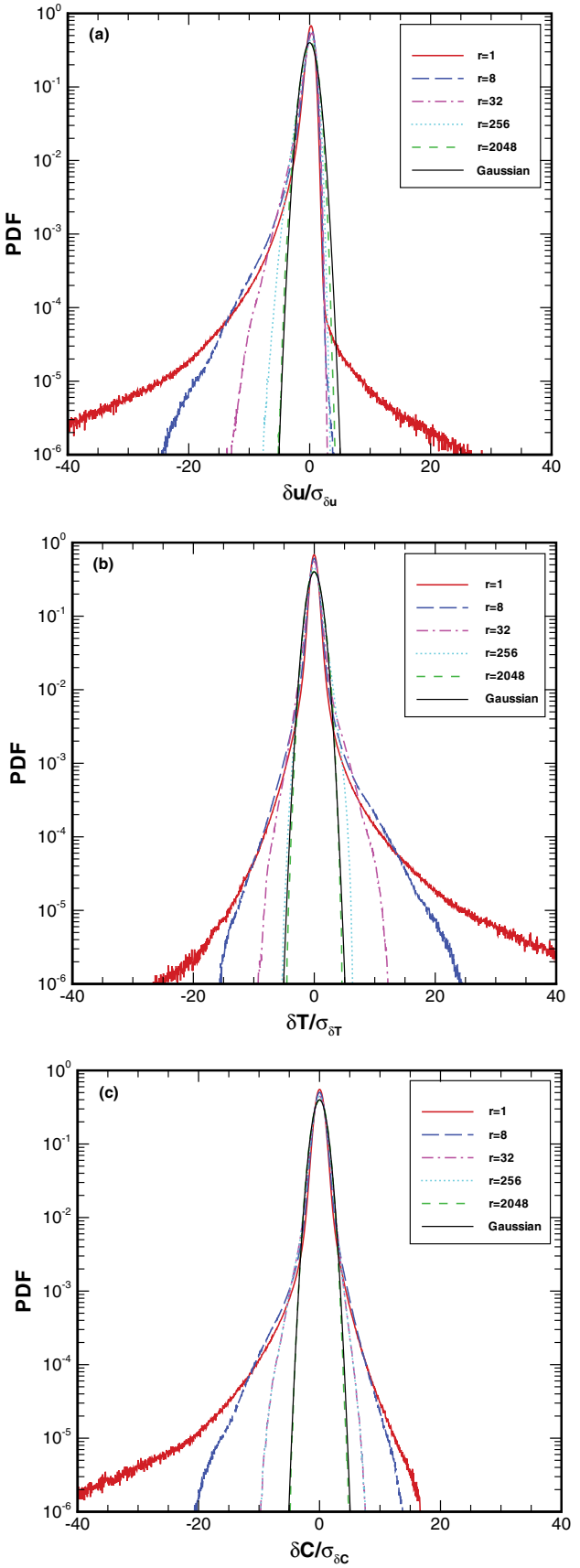

FIG. 5. (Color online) The PDFs for δu, δT, and δC normalized by their standard deviations at different separation distances $r = 1, 8, 32, 256, 2048$.

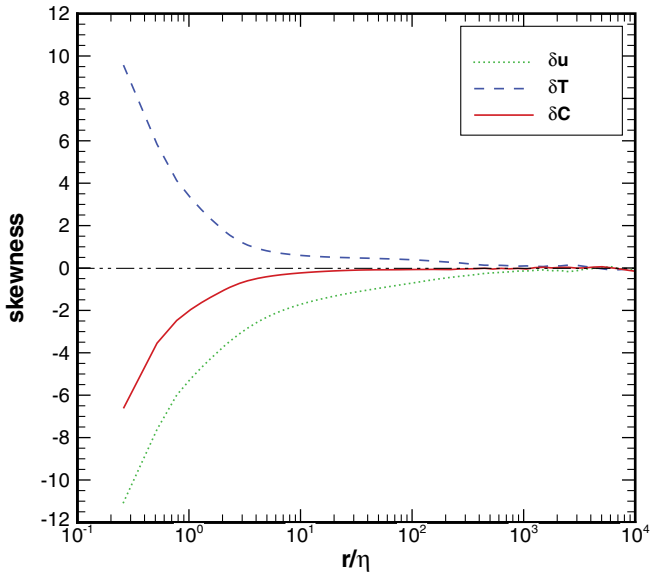

FIG. 6. (Color online) The variations of the skewnesses of the velocity (dotted line), temperature (dashed line), and concentration (solid line) increments against the normalized separation distance.

PDFs all deviate drastically from Gaussian, implying strong intermittencies. Moreover, the PDFs for ξ/σ_ξ and ζ/σ_ζ are negative asymmetric whereas that for θ/σ_θ is positive asymmetric. The skewnesses of ξ, θ and ζ are defined as

$$S_\xi = \frac{\langle \xi^3 \rangle}{\langle \xi^2 \rangle^{3/2}}, \quad S_\theta = \frac{\langle \theta^3 \rangle}{\langle \theta^2 \rangle^{3/2}}, \quad S_\zeta = \frac{\langle \zeta^3 \rangle}{\langle \zeta^2 \rangle^{3/2}}. \tag{3.2}$$

Here, their measured values are $S_\xi = -9.71$, $S_\theta = 8.07$, and $S_\zeta = -4.88$. It is striking that the signs of S_ξ (or S_ζ) and S_θ are opposite, because similar to the concentration, the temperature is advected by the velocity as well. The explanation is that in

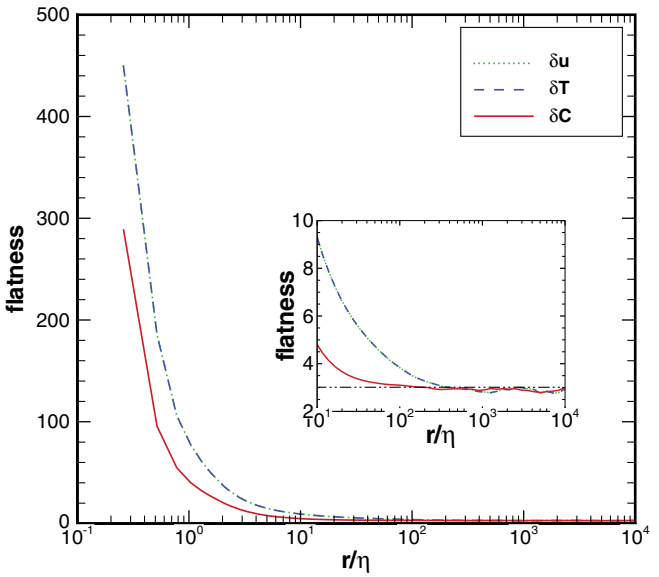

FIG. 7. (Color online) The variations of the flatnesses of the velocity (dotted line), temperature (dashed line), and concentration (solid line) increments against the normalized separation distance. Inset: the same plot in the range of $r/\eta = 10^1 \sim 10^4$.

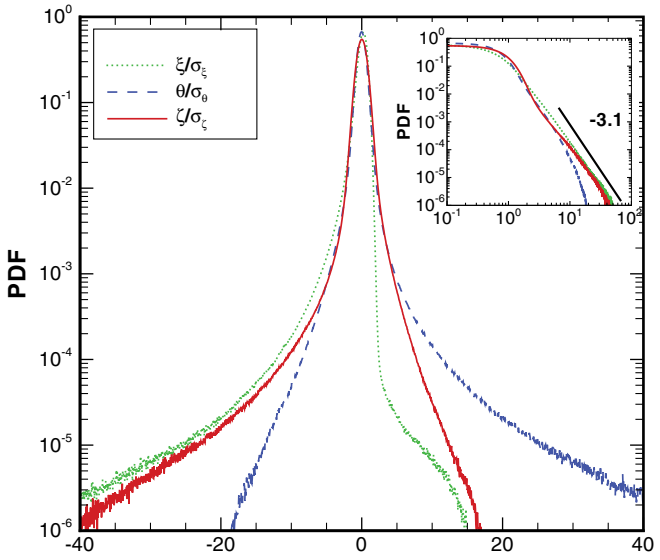

FIG. 8. (Color online) The PDFs for velocity (dotted line), temperature (dashed line), and concentration (solid line) gradients normalized by their standard deviations. Inset: the log-log plot of PDFs for the negative gradients.

the stationary state, the mass continuity equation is reduced to

$$\frac{\partial \rho}{\partial x} = -\frac{\rho \xi}{u}. \tag{3.3}$$

Combining with the isentropic condition $T = \rho^{\gamma-1}$ gives the expression for the ratio of S_θ to S_ξ

$$\frac{S_\theta}{S_\xi} = -\langle \rho^{\gamma-2}\rangle \langle (\rho^{\gamma-2})^2\rangle^{-1/2} \left\langle \left(\frac{\rho}{u}\right)^3 \right\rangle \left\langle \left(\frac{u}{\rho}\right)^2 \right\rangle^{3/2}. \tag{3.4}$$

Based on the fact that both ρ and u are positive, the result of $S_\theta > 0$ is obtained.

In the inset of Fig. 8, we show the log-log plot of the three negative gradients versus their PDFs. It is seen that the power-law exponent values of the PDF tails for the large negative ξ, θ, and ζ are $q_\xi = -3.1$, $q_\theta = -4.1$, and $q_\zeta = -3.0$. In contrast, simulations of the 1D Burgers turbulence driven by various forces give $q_\xi = -3.0, -3.4$, or -3.5 [7,13,33,34]. The major contributions for these tails are from the sawtoothlike shocklets rather than a single strong shock, which is similar to the 3D compressible turbulence [35].

In Fig. 9, we plot the contours of the time-averaged normalized joint PDFs for $(\xi/\sigma_\xi, \theta/\sigma_\theta)$ and $(\xi/\sigma_\xi, \zeta/\sigma_\zeta)$ [i.e., $Q_j(\xi,\theta)$, $Q_j(\xi,\zeta)$]. As we know, the contour shape of the joint PDF for $(\partial_x v, \partial_x w)$ in a linear problem (v,w) is concentric circles [29]. Back in Fig. 9(a), the contour shape of $Q_j(\xi,\theta)$ remarkably deviates from the concentric circles, implying that the feedback on the velocity from the advected temperature leads (u,T) to be a nonlinear problem. In contrast, there is no coupling between the velocity and the advected concentration, making (u,C) a linear problem. Indeed, the contour shape of $Q_j(\xi,\zeta)$ shown in Fig. 9(b) approximately appears as concentric circles.

The maximum positions of the single PDFs shown in Fig. 8 are all origins. In contrast, the maximum positions of $Q_j(\xi,\theta)$ and $Q_j(\xi,\zeta)$ are $(0.3, -0.02)$ and $(0.24, 0.02)$, respectively,

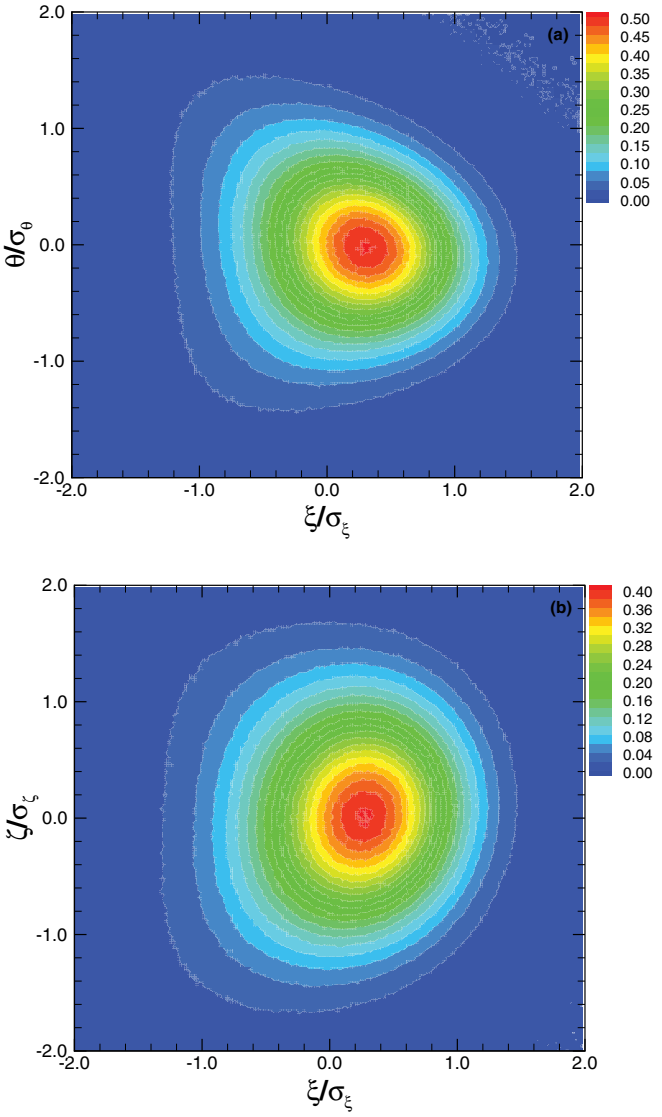

FIG. 9. (Color online) The joint PDFs for the normalized velocity and temperature gradients (a), and the normalized velocity and concentration gradients (b), respectively.

where the transverse drifts $\Delta^a_\theta = -0.02$ and $\Delta^b_\zeta = 0.02$ can be attributed to the numerical errors. Unfortunately, so far we do not know the mechanism for the longitudinal drifts $\Delta^a_\xi = 0.3$ and $\Delta^b_\xi = 0.24$. But it can be still concluded in two respects: (i) the rarefaction wave generates frequently, though the 1D compressible flow is full of the discontinuous sawtooth structures; (ii) the scalar fluctuations in the rarefaction wave region are weak, in other words, most of the strongly variant front structures of scalars arise around the shocks [36,37].

B. Structure function, scaling exponent, and spectrum

The SFs for δu, δT and δC are defined as follows:

$$S^V_p(r) \equiv \langle |\delta u|^p \rangle, \quad S^T_p(r) \equiv \langle |\delta T|^p \rangle, \quad S^C_p(r) \equiv \langle |\delta C|^p \rangle. \tag{3.5}$$

In Fig. 10, we plot S^V_p, S^T_p, and S^C_p against r/η for the order number $p = 2,4,6,8$. For both S^V_p and S^T_p, in the range of

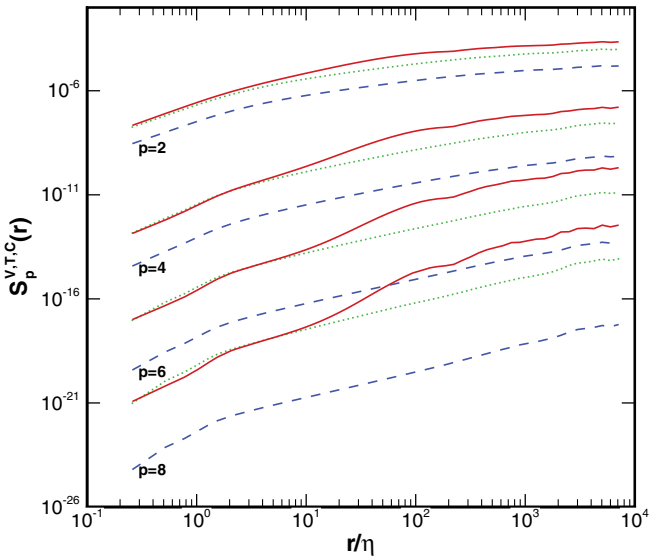

FIG. 10. (Color online) The velocity (dotted line), temperature (dashed line), and concentration (solid line) structure functions against the normalized separation distance.

$2 \leqslant r/\eta \leqslant 200$, the flat regions of finite width are identified, whereas for S_p^C, in the same range, there are two scaling regions in which the local scaling exponents take a local minimum and a local maximum. The crossover occurs in range of $8 \leqslant r/\eta \leqslant 17$. In the range $2 \leqslant r/\eta \leqslant 8$, the local minimum approaches an asymptotic value of $z_p^{C,\min} \approx 1.5$, whereas in the range $17 \leqslant r/\eta \leqslant 200$, the local maximum increases with p but the rate of increase becomes smaller. In Fig. 11, we plot the mixed velocity-temperature SF $S_p^{\mathrm{MT}}(r)$ and mixed velocity-concentration SF $S_p^{\mathrm{MC}}(r)$ against r/η, with their definitions

$$S_p^{\mathrm{MT}}(r) \equiv \langle |\delta u(\delta T)^2|^{p/3} \rangle, \quad S_p^{\mathrm{MC}}(r) \equiv \langle |\delta u(\delta C)^2|^{p/3} \rangle. \quad (3.6)$$

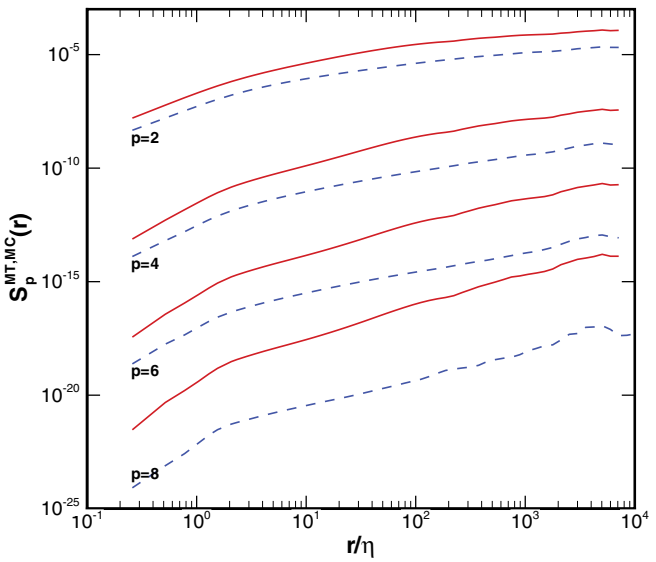

FIG. 11. (Color online) The mixed velocity-temperature (dashed line) and velocity-concentration (solid line) structure functions against the normalized separation distance.

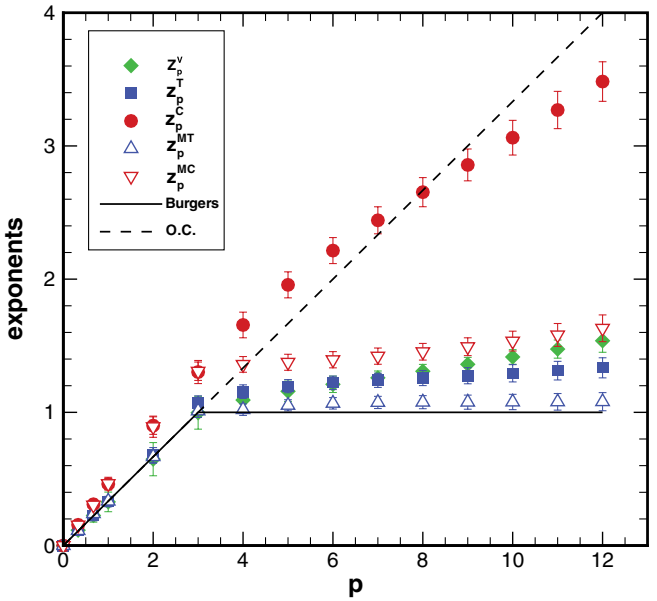

FIG. 12. (Color online) The scaling exponents as functions of the order number. Velocity: diamonds; temperature: squares; concentration: circles; mixed velocity-temperature: triangles; mixed velocity-concentration: gradients. The solid and dashed lines are for the Burgers and Obukhov-Corrsin scalings, respectively.

It is seen that the behaviors of the curves for S_p^{MT} and S_p^{MC} are similar to those for S_p^V and S_p^T. In other words, there are neither local minima nor local maxima in these curves. For S_p^{MT}, in the range of $2 \leqslant r/\eta \leqslant 1000$, the $p = 8$ curve has a flat region of finite width, and the width gradually decreases as p decreases. Similarly, for S_p^{MC}, the flat finite-width region for the $p = 8$ curve locates in the range of $2 \leqslant r/\eta \leqslant 750$, and the width also decreases with decrease in p. This says that for a fixed p, $S_p^{\mathrm{MC}}(r)$ scales with a single power law regardless of whether r/η lies in either $2 \leqslant r/\eta \leqslant 8$ or $17 \leqslant r/\eta \leqslant 200$. This observation motivates the following conjecture: the concentration transfer function at a given p has a single scaling exponent throughout the range of $2 \leqslant r/\eta \leqslant 750$.

The scaling exponents of S_p^V, S_p^T, S_p^C, S_p^{MT}, and S_p^{MC} (i.e., z_p^V, z_p^T, z_p^C, z_p^{MT}, and z_p^{MC}) as functions of the order number p are plotted in Fig. 12, where the solid and dashed lines are for the Burgers and Obukhov-Corrsin (OC) scalings, respectively. These scaling exponents are computed by taking averages of the values of the local scaling exponent curves, which are at plateaus of finite widths, and the corresponding error bars are marked by their standard deviations. It is seen that among z_p^V, z_p^T, and z_p^C, for each p, z_p^T is smallest and close to the Burgers scaling, whereas z_p^C is largest and to some extent approaches the OC scaling. This phenomenon indicates that in the 1D compressible flow, the active temperature is most intermittent, whereas due to the existence of inverse cascade (see below), the intermittency of the passive concentration is weakened. It is also found that z_p^{MC} locates between z_p^V and z_p^C, which is similar to that in the incompressible limit. But it is striking that z_p^{MT} is smaller than both z_p^V and z_p^T, which is also observed in the 3D weakly compressible turbulent flow [38]. This is a topic for future study. Note that the simulation results shown in Fig. 12 are obtained by using a long-time average (about

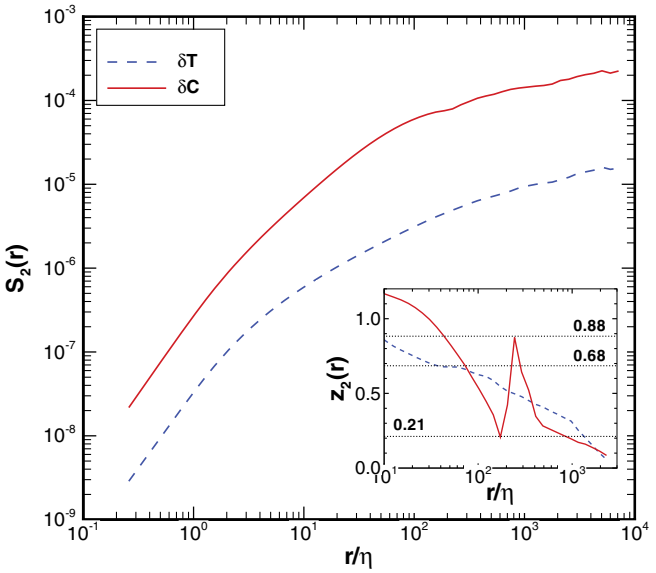

FIG. 13. (Color online) The second-order structure functions of the temperature and concentration increments against the normalized separation distance. Inset: the local scaling exponents for the two structure functions.

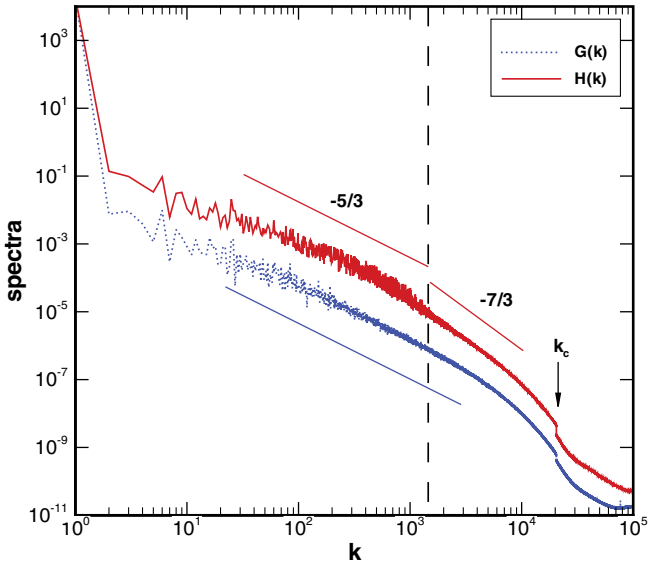

FIG. 14. (Color online) The spectra of temperature and concentration, where k_c is for the cutoff wave number of f_u and f_c.

large-eddy turnover time). In fact, the scalar scaling exponents for each single time frame have intense fluctuations with time, much larger than that of the velocity scaling exponent.

In Fig. 13 we plot the second-order SFs of temperature and concentration [i.e., $S_2^T(r)$ and $S_2^C(r)$] against r/η. According to the Kolmogorov-Obukhov-Corrsin (KOC) theory, both S_2^T and S_2^C scale as $r^{2/3}$. Nevertheless, our simulation results are quite different: in a flat region, the slope of the S_2^T curve slowly varies with r/η. Contrarily, for the S_2^C curve, its slope distinctly changes as r/η increases, and there are two different scaling regions.

To more carefully examine the scaling behaviors of S_2^T and S_2^C, in the inset of Fig. 13 we plot the local scaling exponents $z_2^T(r)$ and $z_2^C(r)$, defined as

$$z_2^T(r) \equiv \frac{d\log\left[S_2^T(r)\right]}{d\log\left(\frac{r}{\eta}\right)}, \quad z_2^C(r) \equiv \frac{d\log\left[S_2^C(r)\right]}{d\log\left(\frac{r}{\eta}\right)}. \tag{3.7}$$

It is found that in the range of $30 \leqslant r/\eta \leqslant 90$, a narrow plateau in the z_2^T curve is identified, with $z_2^T \approx 0.68$, a slightly larger than 2/3. In contrast, starting from $r/\eta = 10$, the z_2^C curve decreases and achieves a local minimum $z_2^{C,\min} = 0.21$ at $r/\eta = 172$, then quickly increases until it achieves a local maximum $z_2^{C,\max} = 0.88$ at $r/\eta \approx 245$, after that, the curve decreases again.

The temperature and concentration spectra are defined as follows:

$$\int_0^\infty G(k)dk = \frac{1}{2}\langle T'^2\rangle, \quad \int_0^\infty H(k)dk = \frac{1}{2}\langle C'^2\rangle. \tag{3.8}$$

We then plot $G(k)$ and $H(k)$ against the wave number k in Fig. 14. It is seen that in the inertial range of about two decades, $G(k)$ obeys a single power-law spectrum $\propto k^{-5/3}$. Contrarily, $H(k)$ can be divided into the so-called inertial-convective and viscous-convective ranges of about two decades and one decade. Their corresponding power-law spectra are $H(k) \propto k^{-5/3}$ and $H(k) \propto k^{-7/3}$, respectively. We point out that the observation on $H(k)$ and $S_2^C(r)$ indicates that there is a one-to-one correspondence between the spectrum and the second-order SF of the concentration.

To investigate the inverse cascade of the passive concentration, we carry out a subensemble decomposition on the velocity by introducing the concept of group velocity difference (GVD) $g(x,r)$

$$\begin{aligned} g(x,r) &= \frac{2}{r}\int_0^{r/2} u(x+r')dr' - \frac{2}{r}\int_{-r/2}^{0} u(x+r')dr' \\ &= \delta\widetilde{u}(x,r/2). \end{aligned} \tag{3.9}$$

The sign of $g(x,r)$ and its association with the rarefaction wave and shock is seen in Ref. [27]. Next, we define the two subensemble SFs according to $g \geqslant 0$ and $g < 0$ as follows:

$$\begin{aligned} S_p^+(r) &\equiv \langle |g \geqslant 0|^p\rangle = \langle |\delta^+\widetilde{u}|^p\rangle, \\ S_p^-(r) &\equiv \langle |g < 0|^p\rangle = \langle |\delta^-\widetilde{u}|^p\rangle. \end{aligned} \tag{3.10}$$

Their scaling exponents $z_p^+(r)$ and $z_p^-(r)$ then are

$$z_p^\pm(r) \equiv \frac{d\log[S_p^\pm(r)]}{d\log\left(\frac{r}{\eta}\right)}. \tag{3.11}$$

In Fig. 15, we plot $z_p^\pm$, z_p^T, and z_p^C as functions of p. For comparison, we plot the Burgers and Kolmogorov (K41) scaling (i.e., z_p^B, z_p^K) as well. This shows that though the values of $z_p^K - z_p^+$ and $z_p^- - z_p^B$ increase with p, z_p^+ and z_p^- are close to the K41 and Burgers scalings, respectively, implying that the $g \geqslant 0$ subensemble has a conspicuous Gaussian property with little intermittency whereas the $g < 0$ subensemble is strongly intermittent. Therefore, the observation of the z_p^T and z_p^C curves separately locating in the Burgers and K41 regimes means that the intermittencies of the active temperature and passive concentration are quite different: strong and weak, respectively.

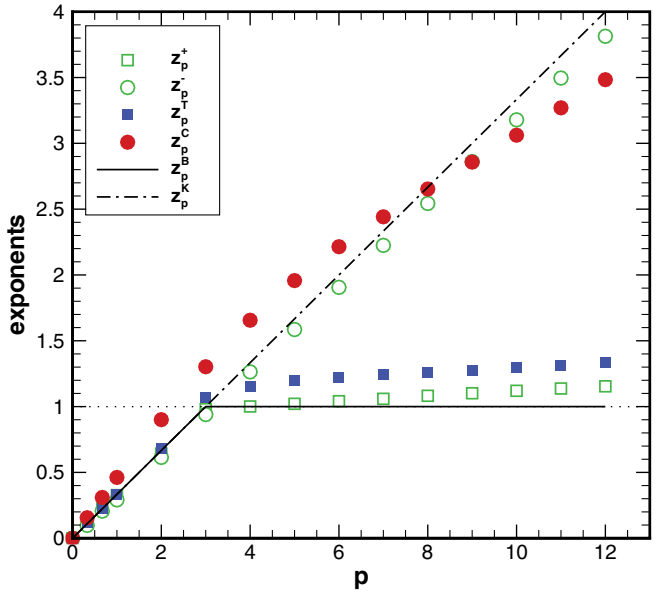

FIG. 15. (Color online) The scaling exponents as functions of the order number. $\delta u > 0$: open squares; $\delta u < 0$: open circles; temperature: solid squares; concentration: solid circles. The solid and dash-dotted lines are for the Burgers and the Kolmogorov scalings, respectively.

In the 1D compressible flow, the strong compressibility makes most of the Lagrangian trajectories of the passive concentration collapse implosively, leading to an inverse cascade of the energy with suppressed intermittency. This means that the flux is negative at large scales. According to Eqs. (2.3) and (2.4), the expressions of the temperature and concentration fluxes in the high Re_λ condition are

$$\Pi_T(x,r) = \left(\gamma - \tfrac{1}{2}\right)\rho T^2 u, \tag{3.12}$$

$$\Pi_C(x,r) = \tfrac{1}{2}\rho C^2 u, \tag{3.13}$$

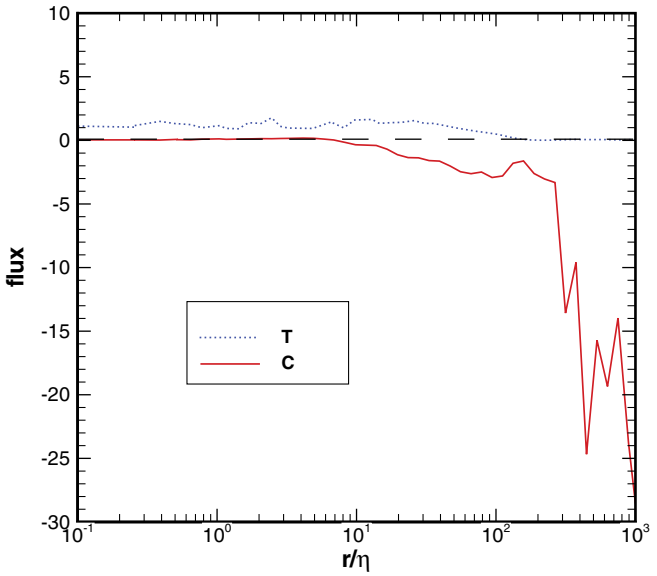

FIG. 16. (Color online) The filtered fluxes of temperature and concentration against the normalized separation distance.

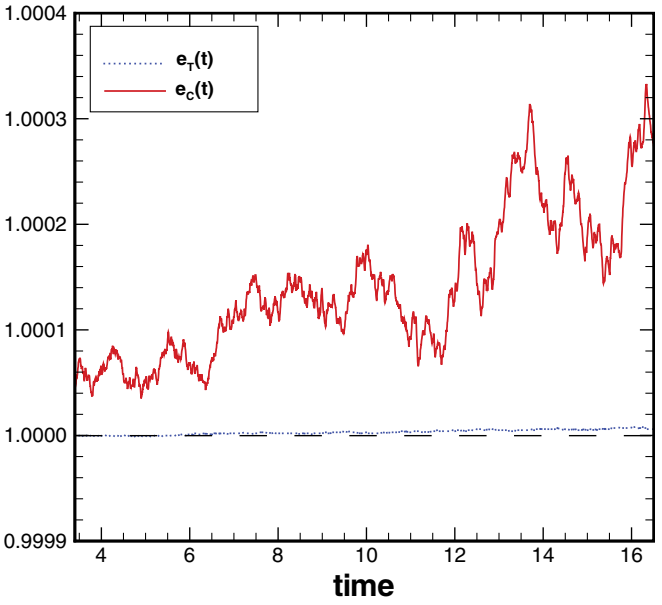

FIG. 17. (Color online) The time evolutions of the total temperature variance $e_T(t)$ and total concentration variance $e_C(t)$.

(see the detailed derivations in the Appendix). Following Eyink's definition [39], we write the filtered versions of Π_T and Π_C as

$$\widetilde{\Pi}_T\left(x,\frac{r}{2}\right) = \left(\gamma - \frac{1}{2}\right)\widetilde{\rho}(\widetilde{T^2} - \widetilde{T}^2)\frac{\partial \widetilde{u}}{\partial x}\left(x,\frac{r}{2}\right), \tag{3.14}$$

$$\widetilde{\Pi}_C\left(x,\frac{r}{2}\right) = \frac{1}{2}\widetilde{\rho}(\widetilde{C^2} - \widetilde{C}^2)\frac{\partial \widetilde{u}}{\partial x}\left(x,\frac{r}{2}\right). \tag{3.15}$$

Now we plot the variations of $\widetilde{\Pi}_T$ and $\widetilde{\Pi}_C$ against r/η in Fig. 16. It is seen that $\widetilde{\Pi}_T$ is positive throughout the whole r/η range, implying that the active temperature always cascades from large to small scales. In contrast, $\widetilde{\Pi}_C$ intersects the zero line at $r/\eta \approx 10$ and then becomes negative, implying that the passive concentration acts direct cascade at small scales ($r/\eta < 10$) but inverse cascade at large scales ($r/\eta > 10$). As a further investigation, the time evolutions for the total variances of the temperature and concentration (i.e., $e_T(t) = \int_0^\infty E_T(k,t)dk$, $e_C(t) = \int_0^\infty E_C(k,t)dk$ [20,32]) are plotted in Fig. 17. We observe that from the initially stationary time $t_0 = 3.4$ to time $t_e = 16.5$, $e_T(t)$ always has small fluctuation around unity, whereas $e_C(t)$ continuously grows. The reason behind this is that for the active temperature, a dissipative anomaly is presented in its downscale cascade and equals the input energy converted from the kinetic energy through viscous dissipation. On the contrary, there is no dissipative anomaly generated in the upscale inverse cascade of the passive concentration. Thus, the input energy from the randomly driving force f_c is accumulated and then makes $e_C(t)$ increase over time.

IV. SUMMARY AND DISCUSSION

In this paper, we carry out the systematically numerical investigation on the statistical behaviors of the active and passive scalars (i.e., temperature and concentration) in the 1D compressible hydrodynamic turbulence. The simulation

is run by using the seventh-order WENO method for space discretization and third-order TVD Runge-Kutta method for time advancement. Simultaneously, the same type of randomly driven all-scale forces are added at the velocity and concentration fields, in order to achieve a stationary state, in which the values of the Taylor Reynolds number and turbulent Mach number are $\mathrm{Re}_\lambda = 2.56 \times 10^6$ and $M_t = 1.0$.

Similar to the Burgers turbulence, the stationary velocity of the 1D compressible flow is consistent with a few large-amplitude and many small-amplitude shocks, and its spectrum is found to be $E(k) \propto k^{-5/3}$ over about two-decade wave numbers. At the same time, the signals of temperature and concentration are full of the small-scale sawtooth structures, and the signals of density and temperature approximately satisfy the isentropic condition.

The PDFs for the fluctuating components of velocity and scalars are computed and compared with the simulation results from 3D NS and Kraichnan flows. It is found that all the three PDFs are Gaussian at the small amplitudes but change into sub-Gaussian at large amplitudes. The PDFs for the velocity and scalar increments at small separation distance are strongly intermittent, and approach Gaussian when the separation distance increases. The features of the PDFs for the velocity and scalar gradients are similar to those for the increments at the small separation distance, such as $r/\eta = 1$. Moreover, the values of the power-law exponents of the PDF tails for the large negative gradients are $q_\xi = -3.1, q_\theta = -4.0$, and $q_\zeta = -3.0$, contrasting to $q_\xi = -3.0$, -3.4, or -3.5 in the various 1D Burgers turbulence simulations. Although the active temperature and passive concentration are both advected by the compressible velocity, their statistical properties are radically different. The passive concentration belongs to the realm of linear problems, whereas the feedback from the active temperature couples the velocity and makes the problem nonlinear. In order to describe this difference, the joint PDFs for (ξ,ζ) and (ξ,θ) are computed and compared. It is found that the contour shape of the former was close to concentric circles, a crucial characteristic for the linear problem, whereas that of the latter is obviously not.

The SFs of the velocity and scalar increments are computed against the separation distance, it is found that both S_p^V and S_p^T have a flat region of finite width, whereas for S_p^C, there are two different regions with a local minimum and a local maximum. Simultaneously, the comparison of the flatnesses between the velocity and concentration increments implies that δu is always more intermittent than δC. As for the mixed velocity-scalar SFs S_p^{MT} and S_p^{MC}, their behaviors are similar to S_p^V and S_p^T. The scaling exponents of the five SFs are computed as functions of the order number p. It is seen that z_p^T is close to the Burgers scaling, whereas to some extent z_p^C approaches the OC scaling, implying that the existence of an inverse cascade remarkably weakens the intermittency of the passive concentration. Furthermore, z_p^{MC} locates between z_p^V and z_p^C, which is similar to that in the incompressible limit, whereas it is striking that z_p^{MT} is smaller than both z_p^V and z_p^T.

Especially, S_2^T has one flat region, whereas there are two regions with a local minimum of 0.21 and a local maximum of 0.88 in S_2^C. This phenomenon is in accordance with the observation in the spectra of the active temperature and passive concentration, where $G(k)$ follows the power law of $k^{-5/3}$, but $H(k)$ can be divided into two different power-law regions: $k^{-5/3}$ and $k^{-7/3}$, implying the coexistence of the inertial-convective and viscous-convective ranges.

Using the subensemble decomposition, the scaling exponents of the positive and negative GVDs (i.e., z_P^+, z_p^-) are computed and compared with z_p^T and z_p^C. It is found that z_p^C is close to z_p^+, implying the existence of the upscale inverse cascade in the passive concentration flux transfer. A further direct proof for this inverse cascade is from the computation of the filtered concentration flux against the separation distance, where $\widetilde{\Pi}_C$ is negative in the range of $r/\eta > 10$. By computing the total variance of the passive concentration, it is confirmed that the absence of the anomaly dissipation in the inverse cascade of the concentration greatly weaken its intermittency, leading the scaling to approach the OC scaling.

To some degree, the simulation results of the 1D compressible turbulence are dependent on their driven forces. For example, there exists differences in the statistics between the all-scale and large-scale forced flows, such as the field signals, energy spectra, and SF scalings [27]. The discrepancy inevitably affects the intermittency of turbulence and thus makes it seem as an artifact of numerics. The unresolved issues include the mechanisms for the large longitudinal drifts in the joint PDFs and the location of the mixed velocity-temperature scaling exponent below its velocity and temperature counterparts. It motivates us to study the statistics of the active and passive scalars in the 3D highly compressible turbulence in the future.

ACKNOWLEDGMENTS

We thank Alessandra Lanotte, Yipeng Shi, Massimo Vergassola, and Jianchun Wang for many useful discussions. This work was supported by the National Natural Science Foundation of China (Grants No. 10921202 and No. 91130001) and the National Science and Technology Ministry under a subproject of the "973" program (Grant No. 2009CB724101). Simulations were run on the supercomputer of Tianhe-1A at the National Supercomputer Center in Tianjin.

APPENDIX: DERIVATIONS OF Π_T AND Π_C

In this appendix, the detailed derivations of Π_T and Π_C are presented as follows. First, we split the total energy equation [Eq. (2.3)] into the kinetic energy and internal energy equations

$$\partial_t \mathcal{E}_\mathcal{K} + \partial_x(\mathcal{E}_\mathcal{K} u) + u\partial_x\left(\frac{p}{\gamma M^2}\right) = \frac{1}{\mathrm{Re}} u\partial_x(\mu\xi) + \rho u f, \tag{A1}$$

$$\partial_t \mathcal{E}_\mathcal{I} + \partial_x(\mathcal{E}_\mathcal{I} u) + \frac{p}{\gamma M^2}\xi = \frac{1}{\mathrm{Re}}\mu\xi^2 + \frac{1}{\alpha}\partial_x(\kappa\partial_x T), \tag{A2}$$

where $\mathcal{E}_\mathcal{K} = \rho u^2/2$ and $\mathcal{E}_\mathcal{I} = \rho T/[(\gamma-1)\gamma M^2]$. Then, we substitute the expression of $\mathcal{E}_\mathcal{I}$ into Eq. (A2)

$$\partial_t(\rho T) + u\partial_x(\rho T) + \gamma\rho T\xi = \frac{\mu}{\mathrm{Re}}\xi^2 + \frac{\kappa}{\alpha}\partial_x^2 T. \tag{A3}$$

Combining Eq. (A3) with Eq. (2.1) gives the temperature equation

$$\rho[\partial_t T + u\partial_x T + (\gamma-1)T\xi] = \frac{\mu}{\mathrm{Re}}\xi^2 + \frac{\kappa}{\alpha}\partial_x^2 T. \quad \text{(A4)}$$

Multiplying both Eq. (A3) and Eq. (A4) by T yields

$$\partial_t\left(\frac{1}{2}\rho T^2\right) + \partial_x\left(\frac{1}{2}\rho T^2 u\right) + (\gamma-1)\rho T^2\xi = \frac{\mu}{\mathrm{Re}}T\xi^2 + \frac{\kappa}{\alpha}T\partial_x^2 T. \quad \text{(A5)}$$

In the inviscid limit, the temperature "energy" conservation recovers, and thus Eq. (A5) has the form of

$$\partial_t\left(\tfrac{1}{2}\rho T^2\right) + \partial_x(\Pi_T) = 0. \quad \text{(A6)}$$

Comparing Eq. (A5) with Eq. (A6), we obtain the expression of Π_T

$$\Pi_T = \frac{1}{2}\rho T^2 + (\gamma-1)\int \rho T^2\xi\, dx. \quad \text{(A7)}$$

The concentration energy equation can be obtained through a similar procedure. Equation (2.4) reads

$$\partial_t\left(\frac{1}{2}\rho C^2\right) + \partial_x\left(\frac{1}{2}\rho C^2 u\right) = \frac{\gamma M^2\chi}{\alpha}C\partial_x^2 C + \rho C f_c. \quad \text{(A8)}$$

In the inviscid limit, the first term in the right-hand side of Eq. (A8) is negligible, therefore, the expression of Π_C is

$$\Pi_C = \tfrac{1}{2}\rho C^2 u. \quad \text{(A9)}$$

[1] J. M. Burgers, *The Nonlinear Diffusion Equation* (Reidel, Dordrecht, 1974).
[2] A. Chekhlov and V. Yakhot, Phys. Rev. E **51**, R2739 (1995).
[3] A. Chekhlov and V. Yakhot, Phys. Rev. E **52**, 5681 (1995).
[4] E. Balkovsky, G. Falkovich, I. Kolokolov, and V. Lebedev, Phys. Rev. Lett. **78**, 1452 (1997).
[5] E. Weinan, K. Khanin, A. Mazel, and Y. Sinai, Phys. Rev. Lett. **78**, 1904 (1997).
[6] S. A. Boldyrev, Phys. Rev. E **55**, 6907 (1997).
[7] T. Gotoh and R. H. Kraichnan, Phys. Fluids **10**, 2859 (1998).
[8] E. Weinan and E. V. Eijnden, Phys. Rev. Lett. **83**, 2572 (1999).
[9] R. H. Kraichnan, Phys. Fluids **11**, 3738 (1999).
[10] E. Weinan and E. V. Eijnden, Phys. Fluids **12**, 149 (2000).
[11] E. Weinan and E. V. Eijnden, Commun. Pure Appl. Math. **53**, 852 (2000).
[12] E. Weinan, K. Khanin, A. Mazel, and Y. Sinai, Ann. Math. **151**, 877 (2000).
[13] S. Boldyrev, T. Linde, and A. Polyakov, Phys. Rev. Lett. **93**, 184503 (2004).
[14] J. Bec and K. Khanin, J. Stat. Phys. **113**, 741 (2003).
[15] J. Bec and K. Khanin, Phys. Rep. **447**, 1 (2007).
[16] Z.-X. Zhang and Z.-S. She, Phys. Rev. E **84**, 026326 (2011).
[17] Ya. B. Zel'dovich, A. Ruzmaikin, and D. Sokoloff, *Magnetic Field in Astrophysics* (Gordon and Breach, New York, 1983).
[18] A. Linan and F. A. Williams, *Fundamental Aspects of Combustion* (Oxford University Press, New York, 1993).
[19] P. Padoan and A. Nordloud, Astrophys. J. **576**, 870 (2002).
[20] A. Celani, M. Cencini, A. Mazzino, and M. Vergassola, New J. Phys. **4**, 72 (2004).
[21] M. Chertkov, I. Kolokolov, and M. Vergassola, Phys. Rev. E **56**, 5483 (1999).
[22] K. Gawedzki and M. Vergassola, Physica D **138**, 63 (2000).
[23] G. Falkovich, K. Gawedzki, and M. Vergassola, Rev. Mod. Phys. **73**, 913 (2001).
[24] J. Wang, L.-P. Wang, Z. Xiao, Y. Shi, and S. Chen, J. Comput. Phys. **229**, 5257 (2010).
[25] S. Gottlieb and C. W. Shu, Math. Comp. **67**, 73 (1998).
[26] W. Sutherland, Philos. Mag. **S5**(36), 507 (1992).
[27] Q. L. Ni and S. Y. Chen (unpublished).
[28] L. Mydlarski and Z. Warhaft, J. Fluid Mech. **358**, 135 (1998).
[29] T. Watanabe and T. Gotoh, New J. Phys. **6**, 40 (2004).
[30] E. Balkovsky and V. Lebedev, Phys. Rev. E **58**, 5776 (1998).
[31] B. I. Shraiman and E. D. Siggia, Nature (London) **405**, 639 (2000).
[32] A. Celani, M. Cencini. A. Mazzino, and M. Vergassola, Phys. Rev. Lett. **89**, 234502 (2002).
[33] J. Bec, U. Frisch, and K. Khanin, J. Fluid Mech. **416**, 239 (2000).
[34] J. Bec, Phys. Rev. Lett. **87**, 104501 (2001).
[35] J. C. Wang, Y. P. Shi, L.-P. Wang, Z. L. Xiao, X. T. He, and S. Y. Chen, Phys. Rev. Lett. **108**, 214505 (2012).
[36] A. Celani, A. Lanotte, A. Mazzino, and M. Vergassola, Phys. Fluids **13**, 1768 (2001).
[37] L. B. Pan and E. Scannapieco, Astrophys. J. **721**, 1765 (2010).
[38] R. Benzi, L. Biferale, R. T. Fisher. L. P. Kadanoff, D. Q. Lamb, and F. Toschi, Phys. Rev. Lett. **100**, 234503 (2008).
[39] G. L. Eyink, Physica D **78**, 222 (1995).